Nanostructured iron oxide thin films deposited by RF sputtering as catalysts for the heterogeneous solar photo-Fenton reaction

(Article begins on next page)

22 November 2024

Nanostructured iron oxide thin films deposited by RF sputtering as catalysts for the heterogeneous solar photo-Fenton reaction

Piera Bosso [a], Regina Del Sole [a], Antonella Milella [a, b,*] , Paolo Mengucci [c], Gianni Barucca [c], Vincenza Armenise [a], Francesco Fracassi [a, b], Fabio Palumbo [b,*]

[a]Dipartimento di Chimica, Università degli Studi di Bari Aldo Moro, Via Orabona 4, 70126 Bari, Italy

[b]CNR-NANOTEC, c/o Dipartimento di Chimica, Università degli Studi di Bari Aldo Moro, Via Orabona 4, 70126 Bari, Italy

[c]Dipartimento di Scienze e Ingegneria della Materia, dell'Ambiente ed Urbanistica – SIMAU, Università Politecnica delle Marche, Via Brecce Bianche 12, 60131 Ancona, Italy

Keywords

Plasma sputtering, iron oxide, photo-Fenton, photocatalytic coatings

*Corresponding Authors:

Antonella Milella, email: antonella.milella@uniba.it; Tel. +39 080 5442858

Fabio Palumbo, email: fabio.palumbo@cnr.it; Tel. +39 080 5442101

Abstract.

Nanostructured iron oxide coatings have been deposited by plasma sputtering by different approaches, with and without thermal annealing, with the aim of preparing supported catalysts for solar photo-Fenton.

1

The chemical and morphological analysis indicate that depending on the experimental conditions the coatings consist of a mixture of γ-Fe$_2$O$_3$ and α-Fe$_2$O$_3$, in variable amounts. Indeed, some of the samples are characterized by elongated nanostructures.

The evaluation of methylene blue degradation in photo-Fenton reaction indicates a good performance of the investigated materials. Degradation percentage between 84 and 97% have been obtained in 180 min with a constant reaction rate as high as 18.0×10^{-3} min^{-1}, with the best result for the sample obtained without thermal annealing. This preliminary investigation highlights that the photoactivity of the coatings is related not only to the content of α-Fe$_2$O$_3$, but also to the presence of developed nanostructures on the coating surface, making the material more active. The proposed method for producing supported catalyst based on photo-Fenton reaction is straightforward, and the possibility to reuse the catalyst up to ten reaction cycles is demonstrated.
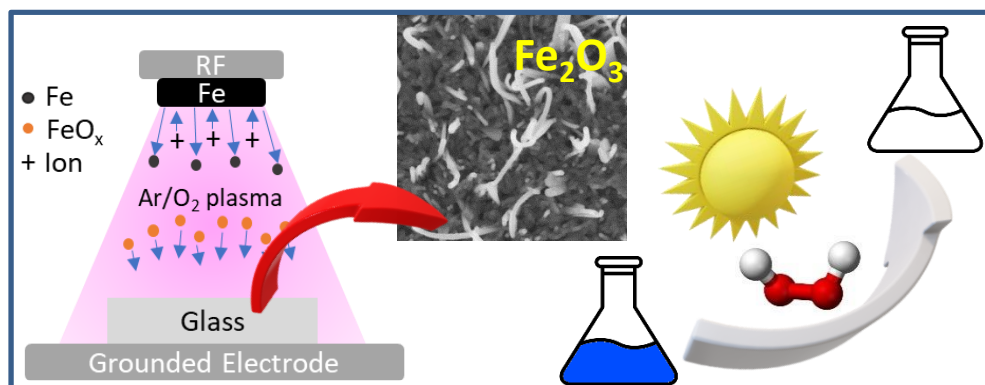
1. Introduction

Advanced oxidation processes (AOPs) are promising water treatment technologies, capable to remove a wide spectrum of organic pollutants from water with high levels of mineralization, under optimized conditions, or at least to transform them into converted to readily degradable small organic molecules.[1-4] A variety of technologies belong to AOPs, having in common the progressive oxidative degradation of the organic contaminants accomplished by highly reactive and oxidizing transitory species (e.g., hydroxyl radical, superoxide radical) generated in situ.[3] Among AOPs, photo-Fenton reaction is considered a cost effective and efficient process to remove several classes of contaminants such as pesticides, dyes, pharmaceuticals and phenols, in presence of H_2O_2 and metal cations [3-6]. This process consists in the combination of the classical Fenton reaction, i.e. the catalysed decomposition of hydrogen peroxide by ferrous iron to produce HO· at low pH, with the photo-assisted regeneration of Fe^{2+} from Fe^{3+}, according to the following equations:

$$Fe^{2+} + H_2O_2 \rightarrow Fe^{3+} + HO^- + HO·$$

$$Fe^{3+} + H_2O + h\nu \rightarrow Fe^{2+} + HO· + H^+$$
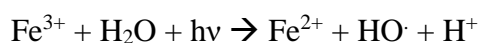
A major advantage of photo-Fenton over other AOPs, such as direct photolysis of H_2O_2 and photoexcitation of TiO_2, is the possibility to use visible light instead of high intensity UV light. However, homogeneous photo-Fenton reaction, mostly performed with inorganic iron salts presents some limitations preventing its widespread application to wastewater treatment: a narrow pH range around 3 is required to ensure that Fe(II) and Fe(III) species exert their catalytic role. [3,6] To this end, real applications include addition of acidifying reagents and a final neutralization step that leads to the precipitation of an iron sludge as iron hydroxides, which needs to be removed after the reaction. [6] Heterogeneous photo-Fenton methods aim to overcome these drawbacks, proceeding at neutral pH and without producing any sludge at the

end of the treatment by using iron-based solid catalysts. The economic and environmental sustainability of this process is increased by the possibility of employing solar energy.[6] It is therefore of great interest the development of inexpensive, efficient and stable photocatalysts able to generate hydroxyl radicals harvesting visible light, since UV light in solar spectrum reaching the earth surface at sea level is limited (nearly 3–4%).

For solar photo-assisted applications, iron(III) oxides are promising photocatalysts.[5] Hematite (α-Fe$_2$O$_3$) is often reported as the active phase, but also other polymorphs have proved to be photoactive.[7-10] Several advantages are offered by these materials, such as a favourable gap value of about 2 eV, large earth-abundance, low cost, non-toxicity, stability in water and under illumination. Since high surface area with large number of active sites is also desirable,[11] various morphological nanostructures were proposed to increase the surface reactivity, such as nanowires, nanocubes, nanosheets, urchin-like structures.[11] Other strategies such as noble metal or graphene doping, composite heterostructures with metals [9,12] or other semiconductors,[12-14] p–n heterojunctions [9,12] and composite [9] were reported for degradation of organic dyes [9,12]. The introduction of other elements, however, could shrink advantages of iron oxide with respect to its cost, earth-abundance and low toxicity, as long as resulting in more complex preparation methods. Fe$_2$O$_3$ catalysts for photo-Fenton water remediation are mostly reported in powder form. However, particles aggregation can occur, due to the magnetic nature of iron oxide, affecting catalyst stability, and formation of slurries as well, not compatible with continuous-flow conditions. Furthermore, powdery catalyst separation, recovering and recycling is an issue and an important cost. Immobilization of the photocatalyst as a coating on a substrate can be an appropriate solution to overcome these limitations, permitting the easy separation and recovery of the catalysts from the treated solutions [3,11]. Therefore, the synthesis of supported catalysts by environmentally friendly preparation methods is a constantly evolving research area. Physical vapor deposition techniques, such as sputtering, allow to deposit thin layers by a one-step process with

homogeneous thickness, good adhesion to the substrate and conformality even on large-area and 3D supports. Nanostructures in different morphology and size can be obtained by tuning deposition parameters.[15,16] Many advantages are offered by this technique, such as not needing any solvent, the possibility to be performed at low substrate temperature and the control of the material stoichiometry by tuning the composition of plasma feed mixture.

Although there are many reports on the degradation of dyes photocatalyzed by iron oxides, long duration, high temperature during the deposition process or post-deposition thermal annealing are usually involved in synthesis protocols for efficient photo-Fenton catalysts. [11,12,15] Mora et al.[14] used TiO_2-Fe_2O_3 multilayers achieving a maximum MB degradation of 67% after 600 min of irradiation. Edla et al.[11] reported the photo-Fenton degradation of methylene blue using hematite nanostructures obtained by thermal annealing (400-600 °C for 4 h) of coating made of metallic iron particulates embedded in H_3BO_3.

Previously, we have reported the plasma sputter deposition of iron oxide based coatings for efficient photoelectrochemical water splitting[17]. In this work, we used a similar approach to prepare all iron-based thin film catalysts for the solar photo-Fenton degradation of methylene blue as model pollutant is addressed. In particular, we present three different routes for the preparation of the iron oxides thin film catalysts with good efficiency and recyclability based on RF sputtering. A comprehensive study of the chemical, structural, morphological, optical and photocatalytic properties of the coatings was performed to assess advantages and disadvantages of each explored method.

2. Experimental

2.1. Film deposition

Three kind of process were considered in this work as illustrated in Figure 1, based on plasma sputtering. Glass was used as substrate for deposition.
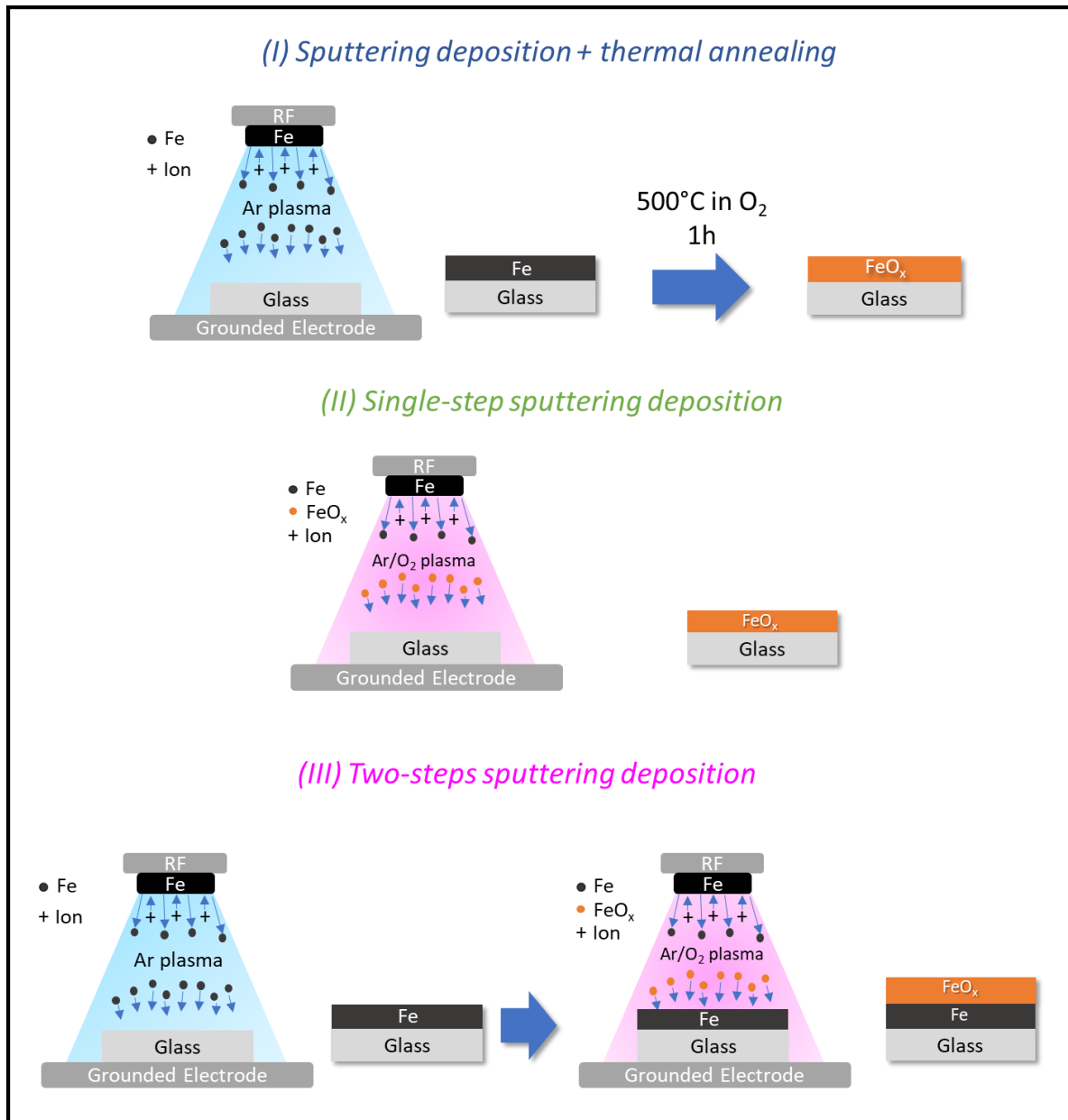

Figure 1. Schematic representation of the different methods employed for the sputtering deposition of iron oxides thin film photocatalysts.

In the first route, a coating was deposited by RF sputtering of an iron target in Ar plasma and a subsequent thermal annealing was carried out for its conversion to oxide (I in Figure 1). As an

alternative, a single-step sputtering process was used to deposit iron oxides films (FeO$_x$) directly from an Ar/O$_2$ plasma (II in Figure 1). In the third approach, a two-steps plasma deposition process was used: a coating was firstly deposited by RF sputtering of an iron target in Ar plasma and, afterwards, an iron oxide overlayer was deposited in situ from direct deposition in Ar/O$_2$ plasma (III in Figure I). Table 1 summarizes the samples prepared and the corresponding experimental conditions.

Plasma sputter deposition processes were conducted in a RF capacitively coupled asymmetric parallel plate reactor, described in a previous work [17]. Briefly, the upper electrode, bearing an iron target (Kurt J. Lesker, 99.9%) was connected to a 13.56 MHz power supply (Cesar 1310, Dressler), through an impedance matching unit. Vacuum in the chamber was achieved through a turbomolecular/rotary pumping system, and the pressure was monitored by a capacitive Baratron (MKS Instruments). Gas flow rates were controlled by electronic mass flow controllers (MKS Instruments), and gas were admitted through a annular shower head located around the top electrode. Glass slides (25 x 25 mm), placed on the ground bottom electrode, 2 cm apart from the powered one, were used as substrate for film deposition. Substrates were cleaned with acetone and ethanol prior to use. Experiments were carried out with argon (0-150 sccm)/oxygen (0-150 sccm) mixtures, so that the total flow was set at 150 sccm, while varying the oxygen percentage between 0 and 100 %. The pressure and the RF power were set at 70 mtorr and 500 W, respectively. The deposition time was set in order to obtain the desired thickness in each condition (1-5 min).

The thermal annealing step was carried out placing the samples on a heated plate in a vacuum furnace in oxygen atmosphere (500 mtorr). Samples were annealed at 500 °C for 60 min with a heating/cooling rate of 10 °C/min.

Table 1. Experimental conditions for the deposition of FeO_x thin film catalysts.

Sample		1st Step			2nd step				
		Plasma deposition			annealing		Plasma deposition		
		Ar (%)	O₂ (%)	Time (min)	T(°C)	Time (min)	Ar (%)	O₂ (%)	Time (min)
Route I	Fe100ann	100	0	1	500	60	//		
	Fe500ann			5					
Route II	FeOₓ50%	50	50	5	//		//		
	FeOₓ100%	//	100	5					
Route III	Fe100/FeOₓ50%	100	0	1	//		50	50	5
	Fe500/FeOₓ50%			5			50	50	
	Fe100/FeOx100%			1			0	100	

2.2. Film characterization

Film chemical characterization was accomplished by X-ray Photoelectron Spectroscopy (XPS). A PHI VersaProbe II (PhysicalElectronics GMBH) with a monochromatic Al Ka source (1486.6 eV) operating with a spot size of 100 µm was used for XPS analysis of the coatings at a take-off angle of 45°, with respect to the surface normal. Survey (0–1300 eV) and high resolution (C1s, O1s, Fe2p, Valence Band) spectra were recorded at a pass energy of 187.85 and 23.95 eV, respectively. Charge correction of the spectra was performed considering the hydrocarbon C1s component (C-C, C-H) as internal reference (Binding Energy, BE=284.8 eV). XRD investigations were caried out by means of a Bruker D8 Advance diffractometer equipped with a θ-θ goniometer in the angular range 2θ= 20° - 70°. Samples were analysed in θ-2θ geometry by using the Cu-kα radiation. Phase identification was achieved by the DIFFRAC.EVA (Bruker AXS) software package via the PDF2 - ICDD (International Centre

for Diffraction Data) database. XRD peak shape analysis was conducted by the OriginPro software vers. 8.5 (OriginLab, Northampton, MA, USA). To obtain quantitative information from the XRD measurements, Rietveld analysis on the whole pattern of selected samples was carried out by using the MAUD software [18].

Rietveld refinement evaluates pattern background, peak shape and Cu-Kα2 radiation. Presence of texture and variation of crystallographic lattice parameters of phases are also estimated in the refinement process.

Rietveld refinement of the whole pattern was carried out by using the crystallographic structure of hematite and maghemite phases available in the database COD (Crystallography Open Database, http://www.crystallography.net/cod/). Instrumental broadening for the specific Bruker D8 Advance equipment used for samples investigations was determined by calibration measurement of Al_2O_3 powder standard.

Film morphology was investigated by scanning electron microscopy (SEM). SEM analyses were carried out using a Zeiss SUPRA 40 field emission scanning electron microscope (FESEM) at the electron acceleration voltage of 3 kV and working distance of 3.0 mm.

Film thickness was measured with an Alpha-Step D-120 stylus profiler on partially masked samples and averaging data over 5 scans.

Optical UV-VIS absorption spectra were acquired in transmission mode on an Agilent Technologies Cary 60 in the range 300-800 nm and at a scan rate of 120 nm min^{-1}. Optical band-gap energies (E_g) were assessed by the Tauc formula:

$$(\alpha h\upsilon)^n = A(h\upsilon - E_g) \ (1)$$

where α is the absorption coefficient, A is a constant, $h\upsilon$ is the incident photonenergy, and n is an exponent, which depends on the nature of the electronic transitions (n =1/2 for allowed indirect transitions). The energy gap was calculated as the interception point between the line fitting portion of the Tauc curve in the proximity of the gap edge and the line representing the background. [19]

The photocatalytic performance in the photo-Fenton reaction was evaluated by monitoring the degradation of methylene blue (MB) dye as a model organic pollutant, using hydrogen peroxide (Sigma Aldrich, 50%) as an oxidizing agent. The catalyst coatings were placed in a beaker with 10 ml of a 10^{-5} M (4 ppm) MB (Alfa Aesar) dye solution and kept in dark under stirring for 15 min to establish adsorption equilibrium between the solution and the catalyst surface. Then the hydrogen peroxide (0.3 M) was added and the visible light source was turned on. A solar simulator lamp (LS0106, LOT-QuantumDesign), equipped with an AM 1.5 G filter, was used as the light source. The solution was kept under stirring and illumination for 180 minutes at a temperature of 20 °C. During the reaction, 150 µl aliquots of MB solution were collected over a time period of 180 min, in order to evaluate the degradation by recording the UV–VIS absorption spectra. The MB concentration was calculated from the intensity of its characteristic peak at 664 nm by means of a calibration curve. The degradation percentage was calculated according to equation 2.

$$\text{Degradation \%} = \frac{C_0 - C_t}{C_0} \times 100 \ (2)$$

The pseudo-first-order rate constant (k) was determined as the negative slope in the plot of the $\ln(C_0/C_t)$ value against irradiation time, where C_0 is the initial concentration and C_t the concentration at time t. Reusability of the films was evaluated by recovering the sample after each degradation reaction and reintroducing it into a fresh dye solution for another experiment (up to 10 times), after washing with distilled water and drying with a nitrogen spray gun.

3. Results and discussion

3.1 Deposition of iron oxide coatings by sputtering and following thermal annealing (route I)

In the first approach, FeO_x thin films are deposited by sputtering of Fe in pure argon plasma and then undergo annealing at 500°C. Two different iron film thickness values were explored (100 nm and 500 nm), to study the different morphology and structure obtained and their photocatalytic performances.

Figure 2 shows the Fe2p and valence band spectra for coatings deposited in pure argon (O_2 = 0%) before (Fe100) and after annealing (Fe100$_{ann}$). The peak position of Fe2p$_{3/2}$ corresponding to metal iron (Fe, 706.9 eV), magnetite (Fe_3O_4, 708.3 eV and 711.0 eV), hematite (α-Fe_2O_3, 709.8 and 710.8 eV) and maghemite (γ-Fe_2O_3, 710.8 eV) are labelled. [20-24]

The as-deposited film (Fe100), is characterized by a spectrum recalling that of magnetite with a maximum around 711.0 eV, relative to Fe (III), and a shoulder at 708.3 eV due to Fe (II).The shoulder at 706.9 eV indicates the presence of metallic iron, as it should be expected from deposition in absence of oxygen. The valence band spectra can be used to provide fingerprint identification of the oxide species.[20, 21] The main features present in the corresponding valence band spectrum are the signal at lowest binding energy ascribable to metallic iron [22] and a broad band at about 5.5 eV typical of magnetite, Fe_3O_4 [20, 21]. This, in turn, confirms that the film deposited in pure argon consists of an iron bulk with a magnetite outermost layer.

After thermal annealing at 500°C (Fe100$_{ann}$), from the Fe2p spectra, the metallic iron signal at 706.9 eV clearly disappears as a result of iron oxidation, as well as, the shoulder at 708.3 eV of magnetite, while the shake-up band indicative of Fe (III) compounds and peaked at about 720 eV appears. Additionally, a change of the signal shape around the maximum, can be observed which is characterized by the presence of two distinct peaks separated by ~1 eV, typical of α-Fe_2O_3. Moreover, the magnitude of the spin–orbit splitting of Fe2p$_{1/2}$–Fe2p$_{3/2}$ (13.7 eV) is that expected for iron (III) oxides and the corresponding valence band spectrum resembles the

hematite one, with three distinct components and a centre at 5.5 eV. [20-24] Finally, upon thermal annealing, the coating turned from black to orange-reddish, which provides a further indication of the occurred transition to hematite.
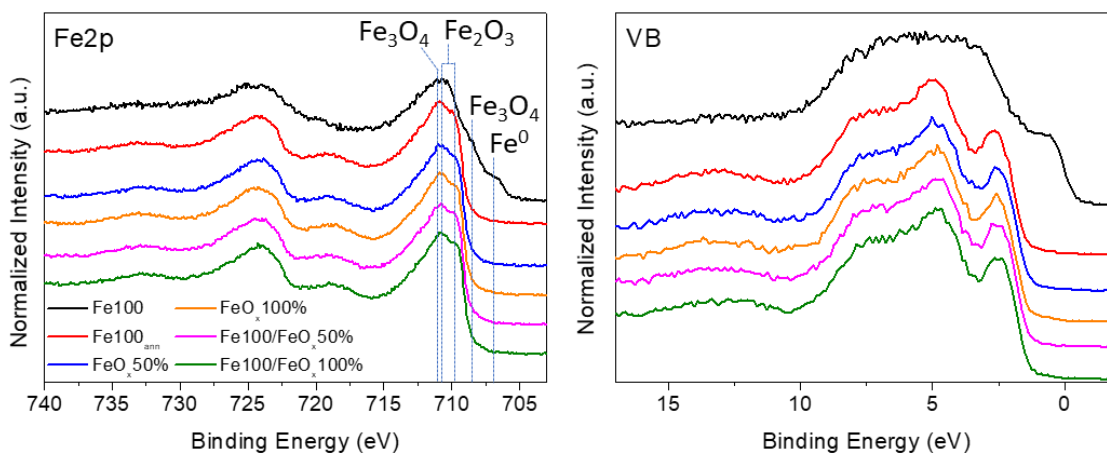

Figure 2. High-resolution XPS Fe2p (left) and Valence band (right) spectra of deposited films.

The outcomes of XPS analyses described for samples Fe100 and Fe100$_{ann}$ also apply to the corresponding thicker ones, Fe500 and Fe500$_{ann}$, and this is reasonable considering the surface sensitivity of XPS analysis. Then, the XPS spectra of these latter samples have not be included in Figure 2.

XRD patterns of samples deposited at 0% of O_2 are reported in Figure 3. The coating not exposed to annealing (Fe100) is single phase metallic iron (Fe Ferrite, ICDD 6-696). Independently on film thickness, after the annealing treatment samples develop crystalline Fe_2O_3 phase in the form of both α- Fe_2O_3 (Hematite, ICDD 33-664) and γ- Fe_2O_3 (Maghemite, ICDD 39-1346), as a result of complete oxidation. Although both iron oxide phases (hematite and maghemite) are present in the annealed samples, intensity and FWHM (Full Width at Half Maximum) of diffraction peaks suggest higher crystallinity for the 500 nm thick coating. Results of the Rietveld refinement carried out on all samples containing both hematite and maghemite are summarized in Table 2. Rietveld refinement allows estimating the relative

12

content of each phase (in wt.%) in the analysed sample, and data confirm the maghemite abundance.
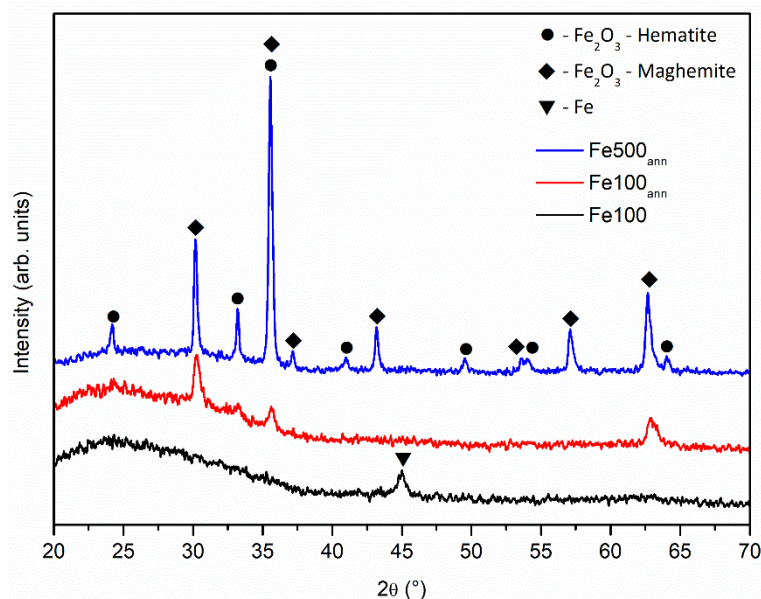

Figure 3. XRD patterns of samples deposited by route I in 0% O_2. Fe100 (black line) is the layer not submitted to the annealing treatment, while Fe100$_{ann}$ (red line) and Fe500$_{ann}$ (blue line) were annealed at 500°C.

Table 2 Results of the Rietveld refinement carried out on all samples containing both hematite and maghemite phases. Phase content is in wt.% and uncertainty reported as provided by the MAUD software.

	Sample	α-Fe$_2$O$_3$ Hematite (wt.%)	γ-Fe$_2$O$_3$ Maghemite (wt.%)
Route I	Fe100$_{ann}$	15 ± 2	85 ± 5
	Fe500$_{ann}$	28 ± 1	72 ± 1
Route III	Fe100FeO$_x$50%	31 ± 2	69 ± 3
	Fe500FeO$_x$50%	42.0 ± 0.6	58.0 ± 0.8

13

The morphology of the coatings was evaluated by SEM. Figure 4 collects the SEM images for iron coatings before and after annealing. The sample Fe100 consists in quasi-spherical structures of 30 nm average diameter. Upon thermal treatment (Fe100$_{ann}$) elongated structures protruding from the surface develop.
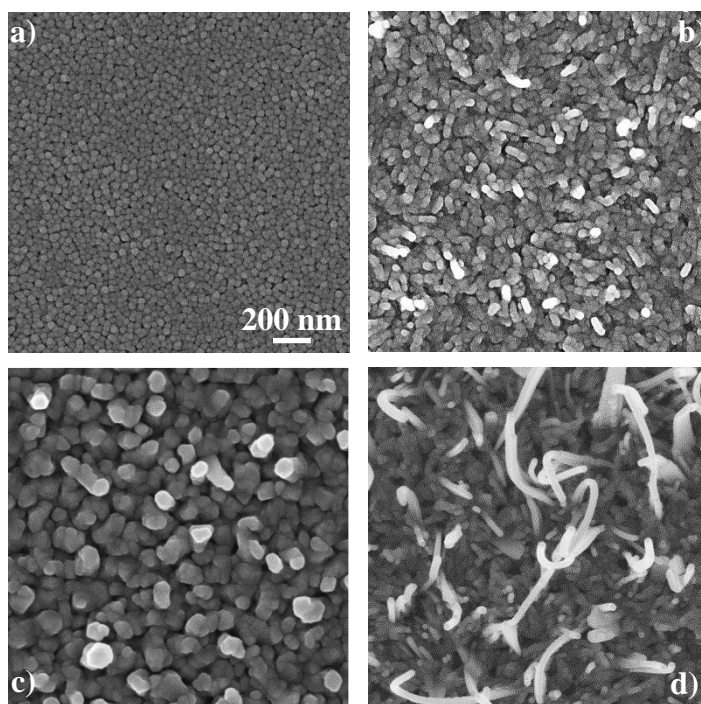

Figure 4. SEM images of thin films deposited by approach I: (a) Fe100, (b) Fe100$_{ann}$, (c) Fe500, (d) Fe500$_{ann}$.

The as-deposited thicker film, Fe500, is more porous showing densely packed nearly-spherical features (up to 90 nm in diameter), eventually resulting in elongated structures. After annealing, substantial morphology modification is observed on sample Fe500$_{ann}$, with nanowires and thicker lamellae formed. For completeness, it is worth reporting that for both films, Fe100 and Fe500, a two-fold increment in the thickness was determined by profilometry measurements, which can be ascribed to the transition from metallic iron to oxide, involving oxygen uptake and a change in the material density.

3.2 Single-step sputter deposition of iron oxide coatings (route II)

14

In this approach, 100 nm-thick films of iron oxide were deposited on glass substrates by RF sputtering of an iron target in Ar/O$_2$ plasmas with different oxygen concentrations, namely O$_2$=50% (FeO$_x$50%) and O$_2$=100% (FeO$_x$100%).

Results on surface chemical composition are reported in Figure 2. Film stoichiometry was determined by calculating the O/Fe ratio from the XPS atomic concentrations, taking into account the amount of oxygen involved into the organic moieties associated with adventitious carbon, according to the procedure described in Ref. [25]. For both films, the O/Fe ratio is equal to 1.5, which is consistent with a Fe$_2$O$_3$ stoichiometry.

XPS Fe2p high resolution spectra of films deposited at different oxygen percentages are shown in Figure 2. Both spectra present features typical of the hematite: (i) the Fe2p$_{3/2}$ maximum shape is characterized by the presence of the two distinct peaks separated by ~ 1eV, as previously discussed; (ii) the magnitude of the spin-orbit splitting of Fe2p$_{1/2}$- Fe2p$_{3/2}$ (13.7 eV) and the presence of the shake-up band at about 718.5 eV is in agreement with iron (III) oxides; (iii) the shape of the valence band spectra are fully indicative of hematite in both conditions. [20-24]

Figure 5 reports the corresponding X-ray diffraction patterns for the one step deposited oxides. All diffraction peaks are due to the rhombohedral α-Fe$_2$O$_3$ phase (Hematite, ICDD 33-664). The coating deposited at O$_2$ =50% shows low preferential growth of (001) crystallographic planes parallel to the substrate. On the other hand, the sample deposited in pure oxygen (O$_2$ =100%) is completely formed of hematite crystals with the (001) lattice planes grown parallel to the substrate. This latter effect is further confirmed by the rocking curve of the layer grown in pure oxygen, which is reported in the inset of Figure 5. In the inset, the black curve is the experimental rocking curve, while the red curve is the result of the peak shape analysis, which allowed to quantify the extent of the texture (FWHM = 3.85±0.05°). Although the same iron oxide phase (hematite) is present in both samples, intensity and shape of diffraction peaks indicate higher crystallization for the layer grown in pure oxygen (FeO$_x$100%).
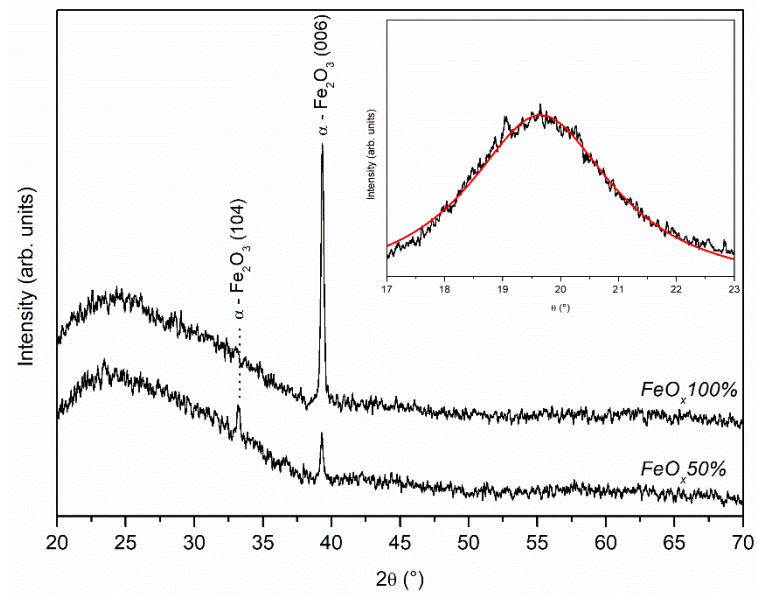
Figure 5. XRD patterns of iron oxide films 100 nm thick deposited at $O_2 = 50\%$ and $O_2 = 100\%$. Inset shows the rocking curve (black line) with superimposed the curve resulting from the peak shape analysis (red line) of the sample deposited in pure oxygen ($FeO_x100\%$).

Figure 6 gathers SEM images of samples $FeO_x50\%$ and $FeO_x100\%$. In both cases morphology is characterized by quasi-spherical structures uniformly distributed with diameter up to 50 nm and 100 nm for oxygen concentration of 50% and 100%, respectively.
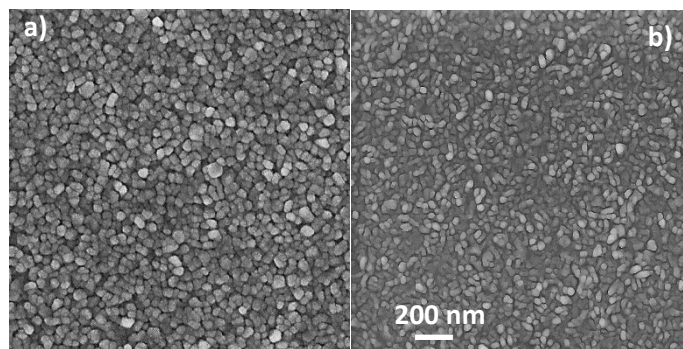

Figure 6. SEM images of samples $FeO_x50\%$ (a) and $FeO_x100\%$ (b).

3.3. Two-steps sputter deposition of iron oxide coatings (route III)

As route I, this third approach consists in two steps: the glass substrate was firstly coated with an iron thin film and then an FeO_x film was deposited in Ar/O_2 plasmas at two different oxygen concentrations (50% and 100%).

The XPS Fe2p and valence band spectra (Figure 2) revealed that the surface chemical composition of the coatings obtained by this process are analogous to those obtained with the single step approach (FeO_x50% and FeO_x100%).

XRD patterns of such coatings are reported in Figure 7. It can be observed that the samples Fe100/FeO_x50% and Fe500/FeO_x50%, when the 2nd step foresees the use of 50% oxygen feed, displays both hematite and maghemite diffraction peaks, without any peak attributable to metallic iron. On the contrary, the XRD pattern of the catalyst Fe100/FeOx100% shows diffraction peaks from the hematite phase only, which grows with a (110) preferential orientation
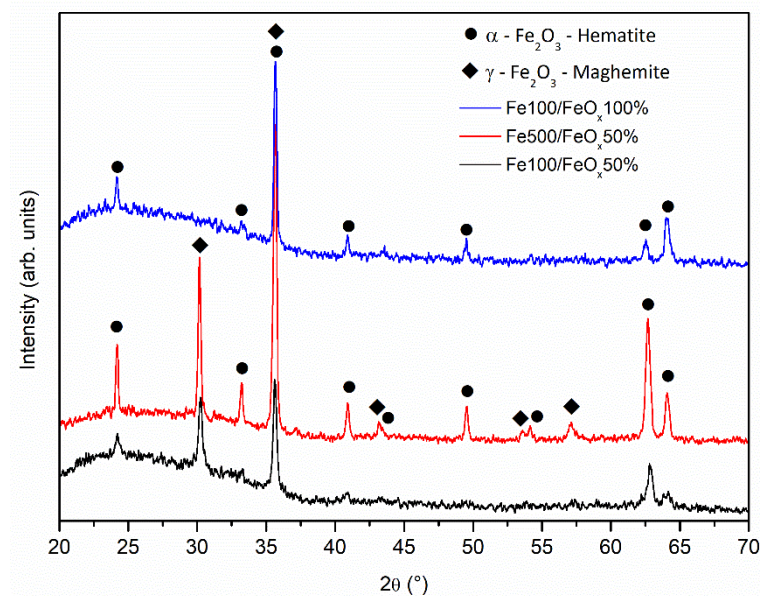

Figure 7. XRD patterns of samples Fe100/FeOx50%, Fe500/FeOx50% and Fe100/FeOx100%.

XRD results indicate that during the second deposition process complete oxidation of the underlying iron film occurs. In order to get insights into this finding, a 100 nm thick iron coating was exposed to an oxygen plasma in the same operational conditions of the second deposition step, but without the iron target attached to the RF electrode. In this case the iron film was converted into magnetite single phase, as assessed by XRD analysis (see supplementary info, Figure S1). Therefore it can be concluded that the conversion of metallic iron into iron oxide was promoted by the second deposition process itself and not by the action of the oxygen plasma. It is tricky to understand the pathway leading to the conversion of the Fe film to Fe_2O_3 , when exposed to the deposition of the second oxide layer. The authors suppose that the direct deposition of the oxide layer, from a plasma fed with Ar/O_2 in presence of a pure iron target, is an exothermic process leaving heat at the surface enough to accelerate the conversion of the sublayer of iron to Fe_2O_3 . However this speculation needs to deeply investigate the process in terms of the energies involved, and it will be object of a following paper. It should be here stressed that, as reported in Table 3, this sample resulted to have no photocatalytic properties, indeed photodegradation percentage and constant rate are similar to the values obtained by H_2O_2 photolysis in the absence of the catalyst.

From Table 2, the Rietveld refinement shows that the total amount of hematite in the samples increases with thickness. However, samples deposited by route III clearly show an enhancement of such effect consequently to deposition of the FeO_x surface layer, and higher amount of hematite phase are obtained.

SEM images, reported in Figure 8, show that the surface of the multilayer coatings presents a mixing of quasi-spherical agglomerates and elongated structures, which become nanowires when the hematite layer is deposited on the 500 nm thick iron layer. As for samples undergoing thermal annealing, the final thickness of these bilayers are double than those expected by simple layer addition, and further demonstrating the phase transition.
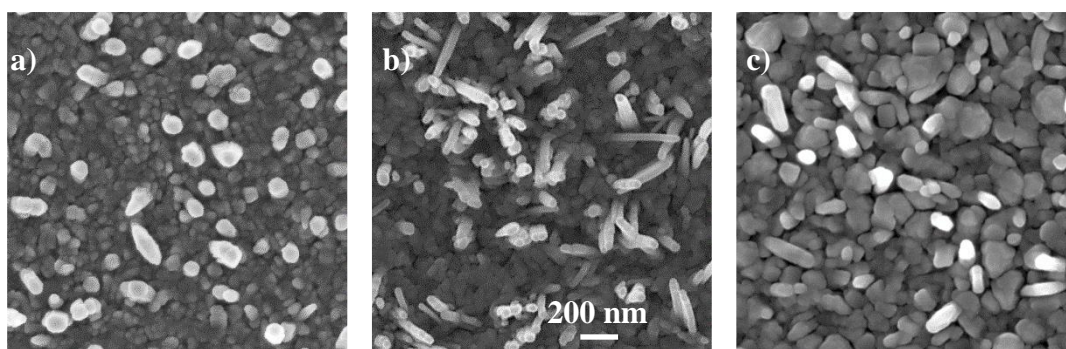
Figure 8. SEM images of two steps sputtered iron oxide coatings: (a) Fe100/FeOx50%, (b) Fe500/FeOx50% and (c) Fe100/FeOx100%.

4. Evaluation of the photocatalytic activity

Since for the application of these films as catalyst for the photo-Fenton degradation of pollutants in water it is central to assess their capability to harvest solar light, their UV-Vis spectra were recorded and processed. Representative absorption spectra and the corresponding Tauc plots are reported in Supplementary Info (Figure S2). The iron films deposited in pure argon are metallic and therefore do not show any energy gap. After thermal annealing, the samples, Fe100$_{ann}$ Fe500$_{ann}$, show UV-Vis spectra similar to the one of hematite, with band gap of 2.0 and 2.1 eV respectively, in accordance with values reported for hematite and maghemite, attesting a conversion of the partially oxidized iron into iron oxide.

Even for samples obtained by routes II and III, the energy gap is consistent with that of hematite with values ranging from 2.0 to 2.2 eV. [26]

The photocatalytic activity of the iron oxide films was evaluated by monitoring the degradation, promoted by solar photo-Fenton reaction, of methylene blue as a model pollutant. Different sets of blank experiments were firstly performed, to exclude other processes to be responsible of the removal of the dye from the solution, namely the absorption on the catalyst surface (dye solution in the presence of the film) and the Fenton reaction (dye solution in presence of film and H_2O_2

in the dark). The concentration of methylene blue did not vary during these experiments in the dark, indicating that these phenomena do not contribute to the pollutant removal.

Figure 9 shows the C_t/C_0 ratio as a function of irradiation time for all the coatings produced. A comparison with results obtained by the H_2O_2 photolysis in the absence of the catalyst is also included. Table 2 summarize the maximum values of photodegradation obtained in 180 min and the relative apparent first order constants.

In all the investigated conditions in presence of the oxide layers the methylene blue concentration decreases with time, reaching in 180 min important degradation percentages, between 84 and 97%, and constant degradation rate in the range 10.2-18.0 x 10^{-3} min^{-1}.
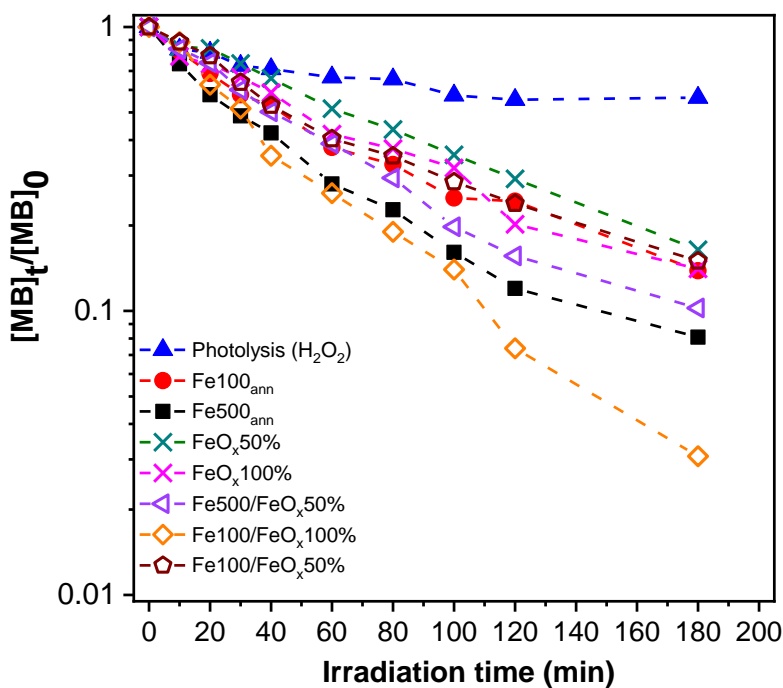

Figure 9. MB relative concentration as a function of irradiation time for the different iron oxide films.

Table 3. MB photodegradation after 180 min of irradiation and pseudo first order constant rate for the different FeO$_x$ photocatalysts.

Sample	Degradation at 180 min (%)	k (x 10^3 min^{-1})
H_2O_2 Photolysis	43± 2	6.7 ± 0.9
Fe100$_{ann}$	86 ± 2	14.7 ± 0.6
Fe500$_{ann}$	91 ± 2	16.2 ± 0.6
FeO$_x$50%	84 ± 2	10.2 ± 0.10
FeO$_x$100%	86 ± 2	11.9 ± 0.5
Fe100/FeO$_x$50%	85 ± 2	12.8 ± 0.4
Fe500/FeO$_x$50%	90 ± 2	16.0 ± 0.2
Fe100/FeO$_x$100%	97 ± 2	18.0 ± 1.6
Fe100/O$_2$plasma	45 ± 2	5.3 ± 0.3

One consideration that can be done is that the photocatalytic activity seems not correlated to the absence of maghemite phase in the coating. On the other hand, the coatings showing the highest degradation percentage and constant rate are characterized by the presence in the morphological structure of protrusions or wire features. This can be ascribed to a higher reactivity of the rougher surfaces, due to a more intimate interaction with the solution.

The coating thickness is not supposed to play a role, since the short hole diffusion length (2-4 nm) and the attenuation length for hematite (in the range 120-46 nm at 550 nm -450 nm) basically confine the reactive events at the topmost surface. [27] However, the main role of thickness seems to be linked to the tendency of thicker coatings to give long protrusions or even wire structures onto the surface upon annealing (route I) or 2nd step deposition in route III, making the catalyst more reactive.

The best photocatalytic performance, in terms of degradation percentage and rate constant, has been found for the two plasma deposition steps sample Fe100/FeOx100%. This result can be explained with an abundant presence of the α phase of iron oxide known to be more active in this photocatalytic process, and sample surface characterized by protrusions, typical of the route III coatings. As a comparison it is possible to consider the one step coating that, albeit being characterized by a α-Fe_2O_3 phase, have a quite flat surface and hence they do not represent the most active catalytic coatings.

Recyclability of the most performing catalyst (Fe100/FeOx100%) has been tested. Figure 10 reports its photocatalytic performance over 10 runs: as it can be seen, no changes in the degradation rate can be observed.
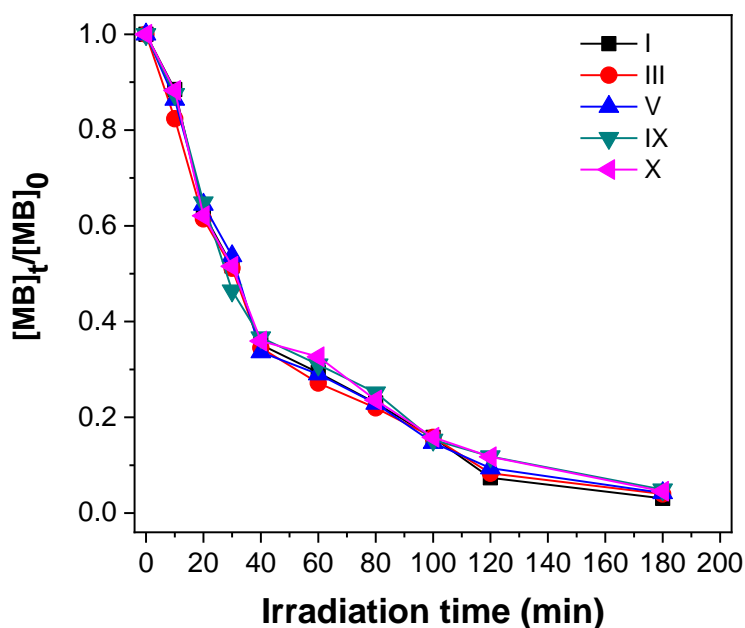

Figure 10. Recyclability over ten cycles of photo-Fenton reaction of the photocatalyst Fe100/FeOx100%.

We must hereby highlight that such coatings are deposited with a quite easy process, and, even in the case of route III, the double step process can be carried out in situ in few minutes. The catalytic performance is comparable with more complex formulations based on particles

functionalization described in literature [28-31]. However, faster reaction rates for particulate based catalysts can also be found [32]. Nevertheless such comparison must take into account that the deposition substrate, in the present study, is continuous and flat, hence less adapt in water photocatalysis. It can be expected that the performance can be improved using large surface area materials, as inorganic membranes, achieving much higher degradation rates.

5. Conclusions

Efficient nanostructured iron oxide supported catalysts for the photo-Fenton degradation of organic pollutants were prepared by different facile and fast processes. The annealing at 500°C of iron coatings with a thickness of 500 nm resulted in nanostructured iron oxide coatings with high photocatalytic properties (degradation percentage of 90%). Single-step deposition in Ar/O_2 mixtures led to well crystallized hematite films with quite good efficiency (photodegradation around 85%).

However, the best photocatalytic performance have been obtained by a double step process, depositing a Fe_2O_3 coating onto a metal iron one. When the overlayer is deposited in pure O_2 plasma, the overall coating consists of α-Fe_2O_3 phase with a surface morphology rich in protruding features that very likely makes the sample more active due to the increased surface area. In fact, the degradation percentage is very close to 100%.

We believe that the photoactivity of the coatings is related both to the content of α-Fe_2O_3, and to the presence of elongated nanostructures on the coating surface, hence also samples rich in maghemite, which is a less active phase, can give photodegradation higher than 85%.

Finally, the most photocatalytic coating has been proven to stand at least 10 photo-Fenton reaction cycles.

It is believed that the performance of similar coatings can be further improved when deposited on large surface area substrates, such as membranes, metal mesh, or scaffolds.

23

Acknowledgement

References

[1] A.V. Vorontsov, Advancing Fenton and photo-Fenton water treatment through the catalyst design, J. Hazard. Mater. 372 (2019) 103–112 https://doi.org/10.1016/j.jhazmat.2018.04.033

[2] M.A. Shannon, P.W. Bohn, M. Elimelech, J.G. Georgiadis, B.J. Marinas, A.M.Mayes, Science and technology for water purification in the coming decades, Nature 452 (2008) 301–310 https://doi.org/10.1038/nature06599

[3] J.L. Wang, L.J. Xu, Advanced Oxidation Processes for Wastewater Treatment: Formation of Hydroxyl Radical and Application, Critical Reviews in Environmental Science and Technology (2012) 42:3, 251-325 https://doi.org/10.1080/10643389.2010.507698

[4] Maria C. Vagi, Andreas S. Petsas, Recent advances on the removal of priority organochlorine and organophosphorus biorecalcitrant pesticides defined by Directive 2013/39/EU from environmental matrices by using advanced oxidation processes: An overview (2007–2018), J. Environ. Chem. Eng, 8 (2020) 102940 https://doi.org/10.1016/j.jece.2019.102940

[5] C. N. C. Hitama, A. A. Jalil, A review on exploration of Fe_2O_3 photocatalyst towards degradation of dyes and organic contaminants, J. Env. Man. 258 (2020) 110050 https://doi.org/10.1016/j.jenvman.2019.110050

[6] L. Clarizia, D. Russo, I. Di Somma, R. Marotta, R. Andreozzi, Homogeneous photo-Fenton processes at near neutral pH: A review, Appl. Catal. B 209 (2017) 358-371 https://doi.org/10.1016/j.apcatb.2017.03.011

[7] Y. Zhang, N. Zhang, T. Wang, H. Huang, Y. Chen Zhaosheng Li, Z. Zou, Heterogeneous degradation of organic contaminants in the photo-Fenton reaction employing pure cubic β-Fe_2O_3, Appl. Catal. B 245 (2019) 410-419 https://doi.org/10.1016/j.apcatb.2019.01.003

[8] Luisa M. Pastrana-Martínez, Nuno Pereira, Rui Lima, Joaquim L. Faria, Helder T. Gomes, Adrián M. T. Silva, Degradation of diphenhydramine by photo-Fenton using magnetically recoverable iron oxide nanoparticles as catalyst, Chem. Eng. J., 261 (2015) 45-52 https://doi.org/10.1016/j.cej.2014.04.117

[9] W. Wu, C. Jiang, V. A.L. Roy, Recent Progress in Magnetic Iron Oxide-Semiconductor Composite Nanomaterials as Promising Photocatalysts, Nanoscale, 7 (2015) 38-58 https://doi.org/10.1039/C4NR04244A

[10] C. Han, L. Machala, I. Medrik, R. Prucek, R. P. Kralchevska, D. D. Dionysiou, Degradation of the cyanotoxin microcystin-LR using iron-based photocatalysts under visible light illumination, Environ. Sci. Pollut. Res. Int 24 (2017) 19435–19443 https://doi.org/10.1007/s11356-017-9566-4

[11] R. Edla, A. Tonezzer, M. Orlandi, N. Patel, R. Fernandes, N. Bazzanella, K. Date, D.C. Kothari, A. Miotello, 3D hierarchical nanostructures of iron oxides coatings prepared by pulsed laser deposition for photocatalytic water purification, Appl. Catal., B 219 (2017) 401–411 https://doi.org/10.1016/j.apcatb.2017.07.063

[12] O. Akhavan, Thickness dependent activity of nanostructured $TiO_2/\alpha\text{-}Fe_2O_3$ photocatalyst thin films, Appl. Surf. Sci., 257 (2010) 1724-1728 https://doi.org/10.1016/j.apsusc.2010.09.005

[13] M. J.Lima, C. G.Silva, A. M.T.Silva, J. C.B.Lopes, M. M. Dias, J. L.Faria, Homogeneous and heterogeneous photo-Fenton degradation of antibiotics using an innovative static mixer photoreactor, Chem. Eng. J. 310 (2017) 342–351 https://doi.org/10.1016/j.cej.2016.04.032

[14] E. S. Mora, E. G. Barojas, E. R. Rojas, R. S. GonzálezMorphological, optical and photocatalytic properties of TiO2–Fe2O3 multilayers. Sol. Energy Mater. Sol. Cells, 91 (2007) 1412-1415 https://doi.org/10.1016/j.solmat.2007.05.010

[15]   Yen-Hua Chen, Kuo-Jui Tu, 2012. Thickness Dependent on Photocatalytic Activity of Hematite Thin Films. Int. J. Photoenergy. 980595, https://doi.org/10.1155/2012/980595

[16]   Z. Zhang, Md. F. Hossain, T. Miyazaki, T. Takahashi, Gas Phase Photocatalytic Activity of Ultrathin Pt Layer Coated on α-Fe_2O_3 Films under Visible Light Illumination, Environ. Sci. Technol. 44, 2010 4741–4746 https://doi.org/10.1021/es1006737

[17]   P. Bosso, A. Milella, G. Barucca, V. Armenise, F. Fanelli, R. Giannuzzi, V. Maiorano, F. Fracassi, Plasma-assisted deposition of iron oxide thin films for photoelectrochemical water splitting. Plasma Process Polym. 18, 2021, 18:2000121 https://doi.org/10.1002/ppap.202000121

[18]   L. Lutterotti, Total pattern fitting for the combined size-strain-stress-texture determination in thin film diffraction, Nucl. Instrum. Methods Phys. Res., Sect. B 268 (2010) 334-340, https://doi.org/10.1016/j.nimb.2009.09.053

[19]   C.S. Garoufalis, P. Poulopoulos, N. Bouropoulos, A. Barnasas, S. Baskoutas, Growth and optical properties of Fe_2O_3 thin films: A study of quantum confinement effects by experiment and theory, Physica E 89 (2017) 67-71 https://doi.org/10.1016/j.physe.2017.02.006

[20]   N. S. McIntyre, D. G. Zetaruk, X-ray photoelectron spectroscopic studies of iron oxides, Anal. Chem. 9 (1977) 1521 https://doi.org/10.1021/ac50019a016

[21]   J. F. Moulder, W. Stickle, P. Sobol, K. D. Bomben, Handbook of X-Ray Photoelectron Spectroscopy: A Reference Book of Standard Spectra for Identification and Interpretation of XPS Data, Physical Electronics, Inc., Eiden Prairie, USA, 1995,

[22]   H. Hochst, S. Hufner, A. Goldmannoch, XPS-valence bands of iron, cobalt, palladium and platinum, Phys. Lett. A, 57A (1976) 265-266 https://doi.org/10.1016/0375-9601(76)90059-1

[23] T. Yamashita, P. Hayes, Analysis of XPS spectra of Fe^{2+} and Fe^{3+} ions in oxide materials, Appl Surf. Sci. 254 (2008) 2441-2449 https://doi.org/10.1016/j.apsusc.2007.09.063

[24] M. C. Biesinger, B. P. Payne, A. P. Grosvenor, L. W.M. Lau, A. R. Gerson, R. St.C. Smart, Resolving surface chemical states in XPS analysis of first row transition metals, oxides and hydroxides: Cr, Mn, Fe, Co and Ni; Appl. Surf. Sci. 257 (2011) 2717-2730 https://doi.org/10.1016/j.apsusc.2010.10.051

[25] B.P. Payne, M.C. Biesinger, N.S. McIntyre, Use of oxygen/nickel ratios in the XPS characterisation of oxide phases on nickel metal and nickel alloy surfaces, Journal of Electron Spectroscopy and Related Phenomena 185 (2012) 159-166 https://doi.org/10.1016/j.elspec.2012.06.008

[26] A. I. Martinez, M. A. Garcia-Lobato, D. L. Perry, Study of the properties of iron oxide nanostructures, in: Armando Barrañón (ed) Research in Nanotechnology Developments, Nova Science Publishers, Inc. Hauppauge 2009, 184-193

[27] P. S. Bassi, Gurudayal, L. H. Wong, J. Barber, Iron based photoanodes for solar fuel production; Phys. Chem. Chem. Phys. 16 (2014) 11834-11842 https://doi.org/10.1039/C3CP55174A

[28] E. da Nóbrega Silva, I. L. Ouriques Brasileiro, V. Stumpf Madeira, B. Aranha de Farias, M. L. Almeida Ramalho, E. Rodríguez-Aguado, E. Rodríguez-Castellón, Reusable $CuFe_2O_4$–Fe_2O_3 catalyst synthesis and application for the heterogeneous photo-Fenton degradation of methylene blue in visible light, J. of Env. Chem. Eng., 8 (2020) 104132 https://doi.org/10.1016/j.jece.2020.104132

[29] L. Suárez, H. Dong, C. Pulgarin, R. Sanjines, Z. Qiang, J. Kiwi, Innovative photo-Fenton catalysis by PE-FeOx films leading to methylene blue (MB) degradation: Kinetics, surface properties and mechanism, Appl. Catal. A. 519 (2016) 68 (ttps://doi.org/10.1016/j.apcata.2016.03.029

[30]   Z-F Cao, X. Wen, P. Chen, F. Yang, X.-L Ou, S. Wang, H. Zhong, Synthesis of a novel heterogeneous fenton catalyst and promote the degradation of methylene blue by fast regeneration of Fe^{2+} , Colloids Surf., A 549 (2018) 94-104 https://doi.org/10.1016/j.colsurfa.2018.04.009

[31]   S. Su, Y. Liu, X. Liu, W. Jin, Y. Zhao, Transformation pathway and degradation mechanism of methylene blue through β-FeOOH@GO catalyzed photo-Fenton-like system, Chemosphere 218 (2019) 83-92 10.1016/j.chemosphere.2018.11.098

[32]   M. Hammad, P. Fortugno, S. Hardt, C. Kim, S. Salamon, T. C. Schmidt, H. Wende, C. Schulz, H. Wiggers, 2021. Large-scale synthesis of iron oxide/graphene hybrid materials as highly efficient photo-Fenton catalyst for water remediation, Environmental Technology & Innovation. 21, 101239. https://doi.org/10.1016/j.eti.2020.101239